Evidence for a meteoritic origin of the September 15, 2007, Carancas crater

A. LE PICHON[*], K. ANTIER[1], Y. CANSI[1], B. HERNANDEZ[1], E. MINAYA[2], B. BURGOA[2], D. DROB[3],
L. G. EVERS[4], and J. VAUBAILLON[5]

[1]Commissariat à l'Énergie Atomique, Centre DAM–Île de France, Département Analyse Surveillance Environnement, Bruyères-le-Châtel,
91297 Arpajon Cedex, France
[2]Observatorio San Calixto, Calle Indaburo 944–Casilla 12656, La Paz, Bolivia
[3]Space Science Division, Naval Research Laboratory, 4555 Overlook Ave., Washington, D.C. 20375, USA
[4]Royal Netherlands Meteorological Institute, Seismology Division, PO Box 201, 3730 AE De Bilt, The Netherlands
[5]Spitzer Science Center, California Institute of Technology, 1200 East California Blvd., Pasadena, California 91125, USA
*Corresponding author. E-mail: alexis.le-pichon@cea.fr

Abstract–On September 15th, 2007, around 11:45 local time in Peru, near the Bolivian border, the atmospheric entry of a meteoroid produced bright lights in the sky and intense detonations. Soon after, a crater was discovered south of Lake Titicaca. These events have been detected by the Bolivian seismic network and two infrasound arrays operating for the Comprehensive Nuclear-Test-Ban Treaty Organization, situated at about 80 and 1620 km from the crater. The localization and origin time computed with the seismic records are consistent with the reported impact. The entry elevation and azimuthal angles of the trajectory are estimated from the observed signal time sequences and back-azimuths. From the crater diameter and the airwave amplitudes, the kinetic energy, mass and explosive energy are calculated. Using the estimated velocity of the meteoroid and similarity criteria between orbital elements, an association with possible parent asteroids is attempted. The favorable setting of this event provides a unique opportunity to evaluate physical and kinematic parameters of the object that generated the first actual terrestrial meteorite impact seismically recorded.

INTRODUCTION

The atmospheric entry of meteoroids can generate infrasonic waves often observed at large distances. In most cases, meteoroids sublimate when they penetrate into the upper atmosphere between an altitude of 60 and 100 km. Larger supersonic objects penetrate deeper into the atmosphere and may be modeled as a line source explosion. Although very large objects, like the Tunguska meteoroid, can generate low-frequency gravity waves, most of them excite acoustic waves in the infrasound domain (ReVelle 1997; ReVelle et al. 1998). Such waves are refracted and channeled over long distances by the temperature gradient and the wind structure of the atmosphere (Kulichkov 1992). Infrasound produced by fragmentations may also be observed a few thousand kilometers away from their origin. At shorter detection distances, the analysis of the recordings presents an opportunity to estimate the entry path, height of thermal bursts, kinetic energy, and other relevant physical characteristics of the meteoroid (Beech et al. 1995; Evers et al. 2001; Brown et al. 2002a; Le Pichon et al. 2002a; ReVelle et al. 2004).

On September 15, 2007, around 16 h 40 min UTC, inhabitants of Desaguadero, near the border of Peru and Bolivia, reported bright lights in the sky moving in a roughly southwest direction (Jackson, personal communication; Macedo et al. 2007). A few seconds later, inhabitants of Carancas, in Peru, heard huge detonations. Damage produced by impacts of ejecta on houses were also reported. Hundreds of meters from this village, a crater was discovered at the coordinates 16.664°S, 69.044°W, and 3826 m altitude. Due to the energy of the impact, mud inside the crater was close to the boiling point. The 13.4×13.6 m nearly circular crater was formed in a few meters of soft, thick brown saturated sediments from the past ice age stand of Lake Titicaca (Macedo et al. 2007). Close to the crater, material was ejected in two main directions: on the southern side (where the rim is 1 m below the northern one, due to the local topography), and also in the north-northwest direction. At larger distances (100 to 200 m), ejecta was found in all directions (Fig. 1). Such a distribution is consistent with the preliminary reported southwestern trajectory (Jackson; personal communication). The water table is about 1.5 m below the surface, and the 5 meter-deep crater quickly filled
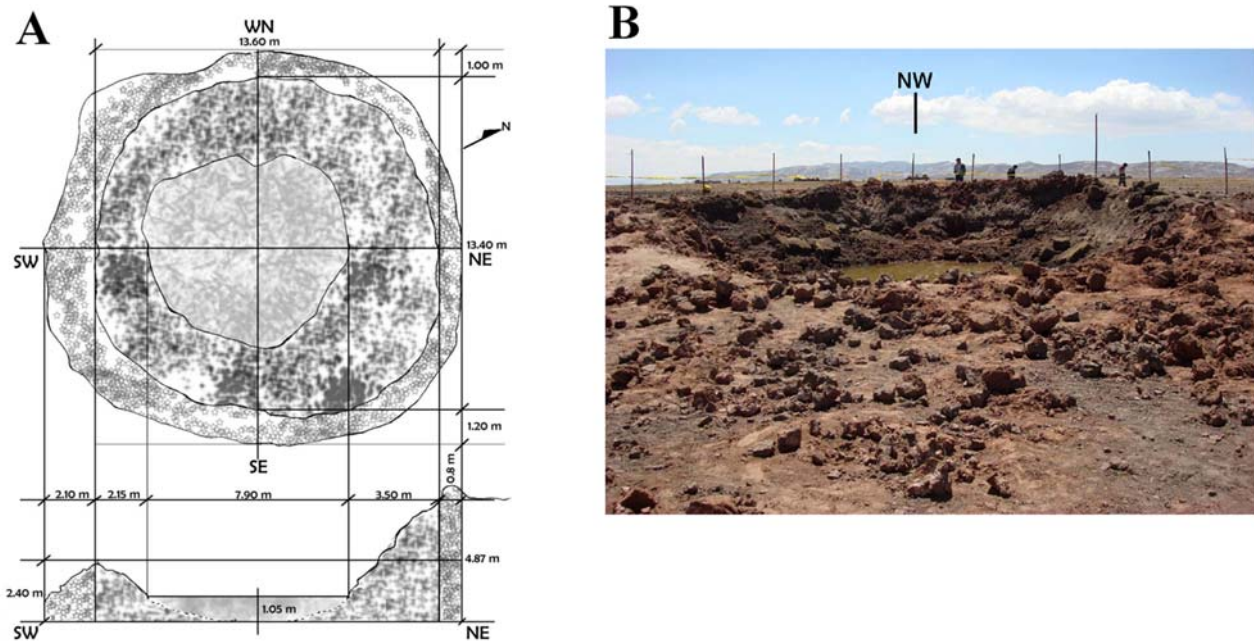
Fig. 1. Views of the crater. A) Global view and transversal section of the crater and its dimensions (13.4 m N-S and 13.6 m E-W) (source: Planetario Max Schreier, adapted from Victor Vallejos, http://fcpn.umsa.bo/fcpn/app?service=external/Planetarium_AreaView&sp=241). B) Photography of the Carancas crater impact (courtesy of Michael Farmer, http://meteoriteguy.com/carancasfallexpedition.htm).

with water, hiding the bottom of the hole and preventing an easy recovery of the main rock fragment remaining from the impact. Fortunately, grey powdering material was found on the rims of the crater, and pieces of the same meteoritic rock were collected tens of meters from it. Their analyses classified it as a H4/5 chondrite type which represents 85% of terrestrial recovered meteorites (Alarcón et al. 2007). Although its size is not exceptional, past studies indicate that a few meter-size meteoroids collide with the Earth every year (Toon et al. 1997; Chyba et al. 1998; Brown et al. 2002b). The most striking characteristic of this rock is thus not its composition, but the fact that it survived its atmospheric entry without major fragmentation (witnesses reported the fall of a single object), and with enough kinetic energy to create the only chondritic impact crater ever observed in recent times.

Usually, most of the meteoroids entering the terrestrial atmosphere suffer from fragmentation before impacting the Earth's surface, breaking the rock into smaller fragments that deposit on the surface, barely causing damages, and even rarely creating craters. The first historical reported crater occurred in eastern Siberia on February 12, 1947, and is associated to the fall of Sikhote-Alin iron meteorite (Krinov 1971). The initial mass of the meteoroid was estimated to be 100 tons. It fragmented in the Earth's atmosphere into small objects. Altogether 122 impact craters were found with diameters ranging from 0.5 to 26 m and with depths ranging from 1 to 12 m. For some similar events, the trajectory can be partially reconstructed, and meteorites recovered. For example, the Park Forest fireball (March 27, 2004)

fragmented three times before reaching the ground (Brown et al. 2004). The Neuschwanstein fireball (April 6, 2002) was also reduced into pieces at the end of its trajectory (Spurný et al. 2003; Oberst et al. 2004; ReVelle et al. 2004), as did the Morávka (May 6, 2000) (Brown et al. 2003), the Tagish Lake (January 18, 2000) (Brown et al. 2002a), and the Peekskill (October 9, 1992) (Beech et al. 1995; Ceplecha et al. 1996) events. Such objects usually produce seismic and acoustic signals when they fragment or when the supersonic front shock sweeps the Earth's surface (Brown et al. 2003).

The implementation of the International Monitoring System (IMS) for the enforcement of the Comprehensive Nuclear-Test-Ban Treaty (CTBT) increases the interest in the identification of naturally occurring events that may result in false alarms. The 60 station infrasound network of the IMS is currently not fully established. However, it has demonstrated its capability for detecting and locating infrasonic sources like meteoroid entries (Arrowsmith et al. 2007). The studied event produced seismic and acoustic signals detected by both a regional seismic network and two IMS infrasound arrays. This paper, supported by high-quality data, aims to reconstruct the trajectory of the meteoroid and to evaluate some of its physical characteristics. In the first part, a detailed analysis of the seismic and infrasound recordings is carried out. If some signals can be attributed to fragmentation, others are undoubtedly associated with the impact, which is a phenomenon that has never been recorded until now. In the second part, from the observed arrival times of seismic phases, the location and origin time of the impact are calculated with a high degree of certainty. Following the

Table 1. Seismic and infrasound stations characteristics. Name, coordinates, distance from the crater, and true back-azimuth of the seismic sensors (LPAZ, BBOB, BBOD, BBOE, BBOK, MOC, and SIV) and the two IMS infrasound arrays (I08BO-Bolivia and I41PY-Paraguay) that provided data.

Station	Longitude (°W)	Latitude (°S)	Elevation (m a.s.l.)	Distance (km)	Back-azimuth (°)
BBOD	68.60	16.64	4235	47	266.9
I08BO	68.45	16.21	4131	80	231.7
LPAZ (PS06)	68.13	16.29	4095	105	246.9
BBOB	68.13	16.14	3911	112	239.2
BBOE	67.98	16.81	4325	114	278.4
BBOK	67.87	16.58	4638	125	265.7
MOC	65.64	21.25	621	621	324.2
SIV (AS08)	61.07	15.99	849	854	263.9
I41PY	57.31	26.34	164	1617	309.1

impact localization, the elevation and arrival angles of the meteoroid path are determined from propagation modeling of infrasonic waves in a realistic atmosphere. In the last part, additional analyses cover source energy estimates from several independent empirical approaches and we discuss possible association with parent asteroids.

OBSERVATIONS

The Carancas meteoroid entry produced infrasonic waves that have been recorded by two IMS infrasound arrays: I08BO in Bolivia located on the Altiplano and I41PY in Paraguay, 80 km northeast and 1617 km southeast of the crater, respectively (Fig. 2). Each of these arrays is composed of four microbarometers, 0.8 to 2.5 km apart. Sensors are MB2000 microbarometers that can measure pressure fluctuations from 0.003 up to 27 Hz. The electronic noise level is 2 mPa rms in the 0.02–4 Hz frequency band over a dynamic range of 134 dB. In order to minimize pressure changes due to surface wind effects, each sensor is connected to an 18-meter-diameter spatial noise reducing system (Alcoverro et al. 2005). A large meteoroid entry is also likely to produce ground coupled airwaves that can be recorded in seismic stations (Cates et al. 2001; Arrowsmith et al. 2007). Such seismic signature has been observed on signals recorded by the Bolivian seismic network operated by the Observatory San Calixto (OSC) in La Paz (Minaya et al. 2007). This network is composed of four vertical short-period stations (BBOB, BBOD, BBOE, BBOK), two three-component short-period stations (LPAZ, MOC), and one three-component short-period and long-period station (SIV). LPAZ and SIV also refer to the primary PS06 and auxiliary AS08 IMS seismic stations, respectively (Fig. 2). Table 1 provides the coordinates and locations relative to the crater of the studied seismic and infrasound stations. In total, five seismic stations, 47 km to 125 km away from the crater, recorded seismic waves from the meteoroid entry and impact.

Figure 3 shows the successive wave trains recorded simultaneously on the two infrasound arrays and the five seismic stations. The first and last detected arrivals (at BBOD and I41PY, respectively) are separated by a nearly 90 min. time delay (Table 2). The comparable seismic recordings at BBOD, BBOE, and BBOK present two clear onsets, while at BBOB and LPAZ, signals are more complex and noisy and do not allow a clear phase identification. The seismic phases marked by the red triangles are consistent with energy originating from the impact location. The difference of few tens of seconds between the observed and the predicted ground coupled airwave arrival times definitely excludes that these arrivals, as well as the second arrival recorded at I08BO, are associated with the impact.

The wave parameters of the acoustic arrivals measured at I08BO and I41PY are calculated with the Progressive Multi-Channel Correlation (PMCC) method (Cansi 1995) (Fig. 4). At I08BO, two transient signals of peak-to-peak amplitude 1.7 and 0.9 Pa, are detected with values of horizontal trace velocity (0.345 km/s) larger than the sound speed at the ground level (0.333 km/s), which indicates a wave propagation with a ~15° shallow elevation angle. The back-azimuth of the first arrival is compatible with acoustic waves originating from the impact. Conversely, even taking into account propagation effects and uncertainties in wave parameter calculations, the back-azimuth of the second arrival (~15° larger than the expected bearing) can not be associated to it. Simple geometrical considerations regarding the path of the meteoroid relative to the location of I08BO suggest that shock waves or thermal bursts can explain the second arrival if the arrival azimuth of the trajectory (clockwise from North) is greater than 53° (section Source Model and Trajectory Reconstruction). At I41PY, 1617 km away from the crater, two signals of much weaker amplitude (20 and 40 mPa) are detected. Both arrival times and back-azimuths are consistent with energy propagating in the stratospheric duct (section Long-Range Propagation). Table 3 summarizes the main characteristics of the detected coherent wave trains at I08BO and I41PY.

TRAIL IN THE ATMOSPHERE AND IMPACT

Atmospheric Specifications and Phase Identification

It is important to account for wind conditions to match the predicted arrivals with the observed signals, as
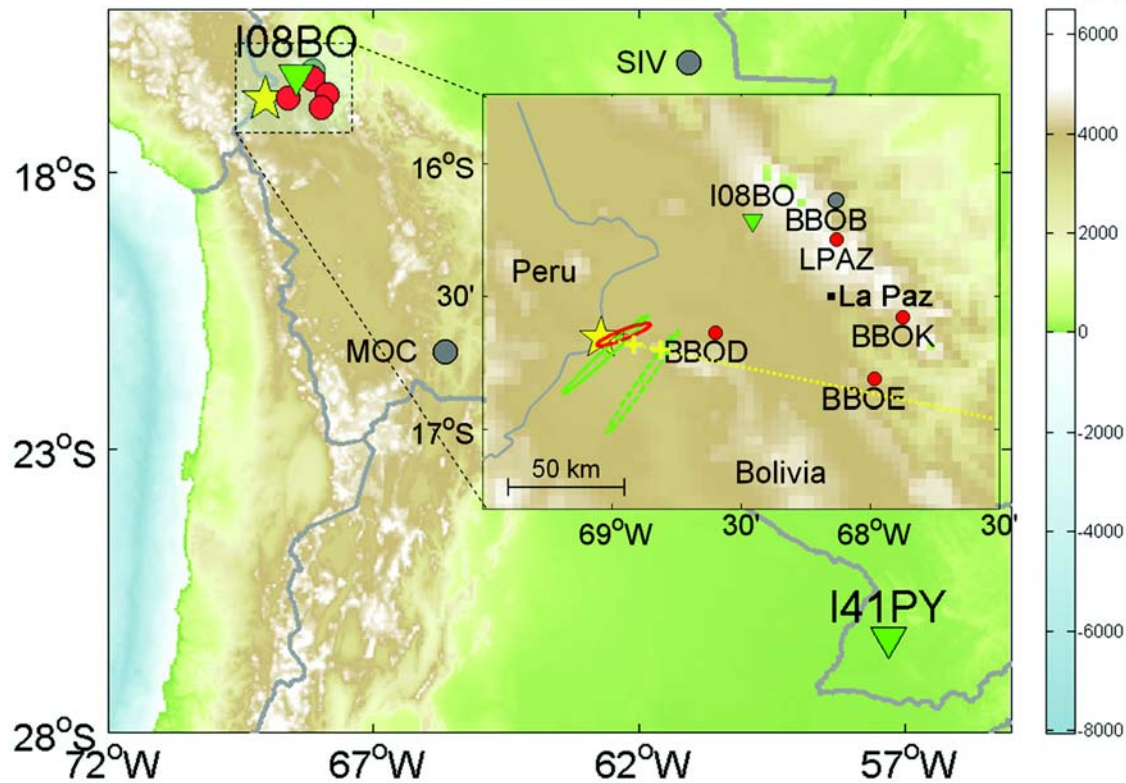
Fig. 2. Location of the Bolivian seismic network and the two I08BO-Bolivia and I41PY-Paraguay infrasound arrays. The yellow star indicates the meteorite impact (16.664°S and 69.044°W, elevation: 3826 m a.s.l.) (Macedo et Macharé 2007). Red circles indicate stations where signals were clearly detected. At BBOB, MOC and SIV (grey circles), no clear ground coupled airwaves have been observed. The red 95% confidence ellipse refers to the impact localization using the observed seismic arrivals on BBOD, LPAZ, BBOB, BBOE, and BBOK (Table 2). The green ellipses refer to cross-bearing localizations with the first and second infrasound arrivals detected at I08BO and I41PY (Table 3). The yellow dashed line indicates the trajectory reconstructed from the observed signals (Fig. 3). The two yellow crosses indicate possible explosions at altitudes of 21 and 31 km as discussed in the section Trail in the Atmosphere and Impact.

fluctuations in the sound speed are generally much smaller than wind variations in the upper atmosphere. Wind and temperature profiles used in our simulations are provided by the European Centre for Medium-Range Weather Forecasts model (ECMWF, http://www.ecmwf.int) from the ground to about 85 km altitude, and the MSISE-90 and HWM-93 empirical reference models (Hedin 1991; Hedin et al. 1996) for higher altitudes. At the time of the event and in the vicinity of the source region, the wind profiles exhibit a rich vertical structure (Fig. 5). Due to the increase of the effective sound speed (sound speed corrected for the horizontal wind terms in the direction of propagation), stratospheric returns are expected for an azimuth ranging from 70 to 270°.

Depending on the atmospheric wind structure, infrasonic waves may propagate in different acoustic wave guides between the ground and tropopause, stratopause, and lower thermosphere (Brown et al. 2002; Garcés et al. 2002). Multiple arrivals, referred to as phases, may then be recorded. They correspond to a specific family of ray paths and turning heights, and are characterized by specific ranges of frequency, amplitude, horizontal trace velocity, and arrival azimuth along the array beam:

(i) Thermospheric phases correspond to infrasonic waves trapped between the lower thermosphere and the ground. Given the strong temperature gradient above 90 km, thermospheric paths are always predicted. However, due to the low particle density and non-linear dissipation in the upper atmosphere, thermospheric returns are strongly attenuated and may not always be observed at large distances (Sutherland et al. 2004). The low elevation angle and relatively high frequency content of signals (above 1 Hz) detected at I08BO and I41PY are incompatible with such phase identification.

(ii) Infrasonic waves trapped between the ground and the stratopause, referred to as stratospheric phases, can propagate efficiently for thousands of kilometers. Their existence mainly depends on the latitude and the season, and fluctuates with the passing of storms and other large-scale atmospheric disturbances (Drob et al. 2003). At the time of the event, in the direction of I41PY, the increase in the effective sound speed in the stratopause is large enough to favor stratospheric returns (Figs. 5 and 7).

(iii) Phases associated with waves refracted from the troposphere strongly depend on local atmospheric conditions. They usually propagate with a celerity (horizontal distance divided by travel time) close to the sound speed near the
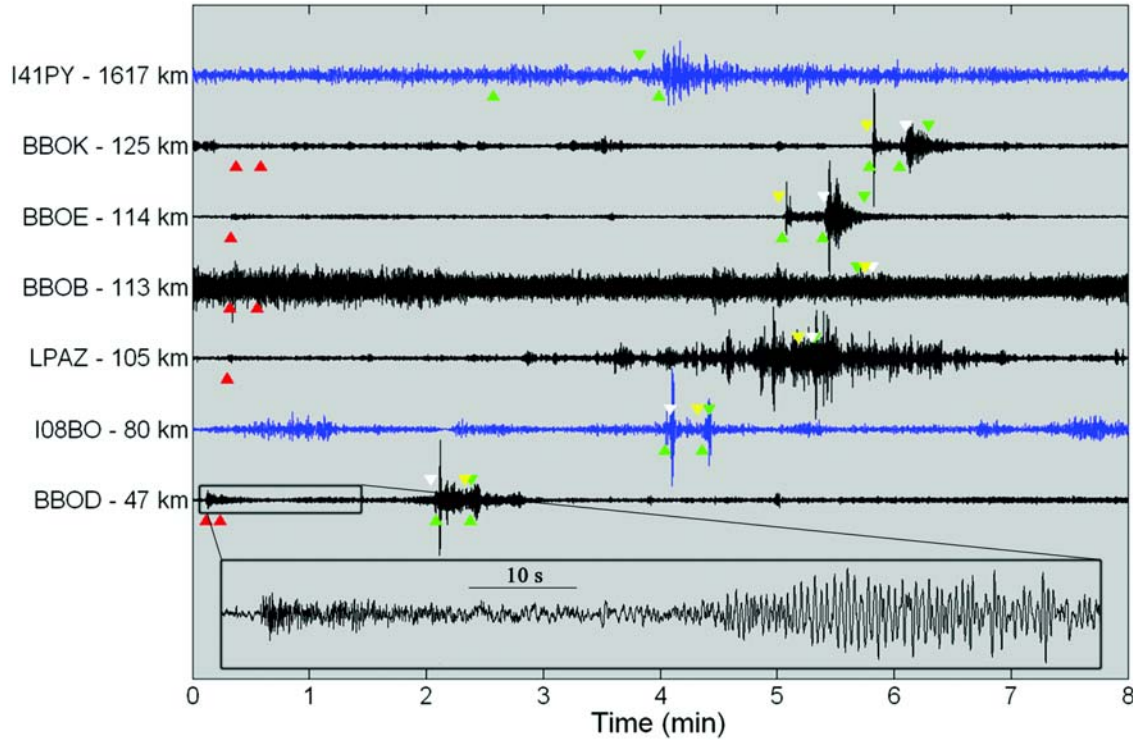
Fig. 3. Waveforms (normalized amplitude) at the I08BO and I41PY infrasound arrays (phase aligned traces in blue) band-pass filtered from 1 to 4 Hz, and short-period vertical seismometers part of the Bolivian seismic network (in black). For all recordings, time is relative to the time of impact t0 (16:40:17 UTC) except for I41PY (t0 + 86 min). At the bottom of the figure, a zoom on the unfiltered recording at BBOD is embedded. This plot indicates a low frequency arrival typical of surface wave from shallow event. The upward-pointing red and green triangles indicate onset times of regional seismic and acoustic waves (infrasound for I08BO and I41BY, and ground coupled airwaves for seismic stations), respectively (Table 2). The downward-pointing green triangles indicate the theoretical arrival times of acoustic waves propagating from the impact location to all receivers with a celerity of 0.33 km/s (with a nearly horizontal propagation), except for I41PY (celerity of 0.30 km/s typical of a stratospheric propagation). The downward-pointing white and yellow triangles refer to the predicted arrival times of acoustic waves generated by two explosions (21 and 31 km above the ground level, respectively) along a trajectory of arrival angle 110° and elevation 50°.

Table 2. Observed arrival times of regional seismic waves, ground coupled airwaves on seismic sensors (sampling rate of 50 Hz) and infrasonic waves at I08BO and I41PY (sampling rate of 20 Hz). Arrivals I1 and I2 do not necessarily originate from the same part of the trajectory of the meteoroid. The notation n.d. (not detected) means the phases were not picked.

Station	Pg	Sg	I1	I2
BBOD	16:40:23.5	16:40:30.9	16:42:22	16:42:41
I08BO	n.d.	n.d.	16:44:10	16:44:34
LPAZ	16:40:35.4	n.d.	Unclear	
BBOB	16:40:35.8	16:40:49.9	Noisy	
BBOE	16:40:36.3	n.d.	16:45:21	16:45:41
BBOK	16:40:39.2	16:40:52.0	16:46:05	16:46:21
I41PY	n.d.	n.d.	18:08:51	18:10:10

Table 3. Main characteristics of the detected coherent acoustic waves at I08BO and I41PY. With a sampling rate of 20 Hz, the expected numerical resolution at 1 Hz is of the order of 0.5° for the azimuth and 5 m/s for the horizontal trace velocity.

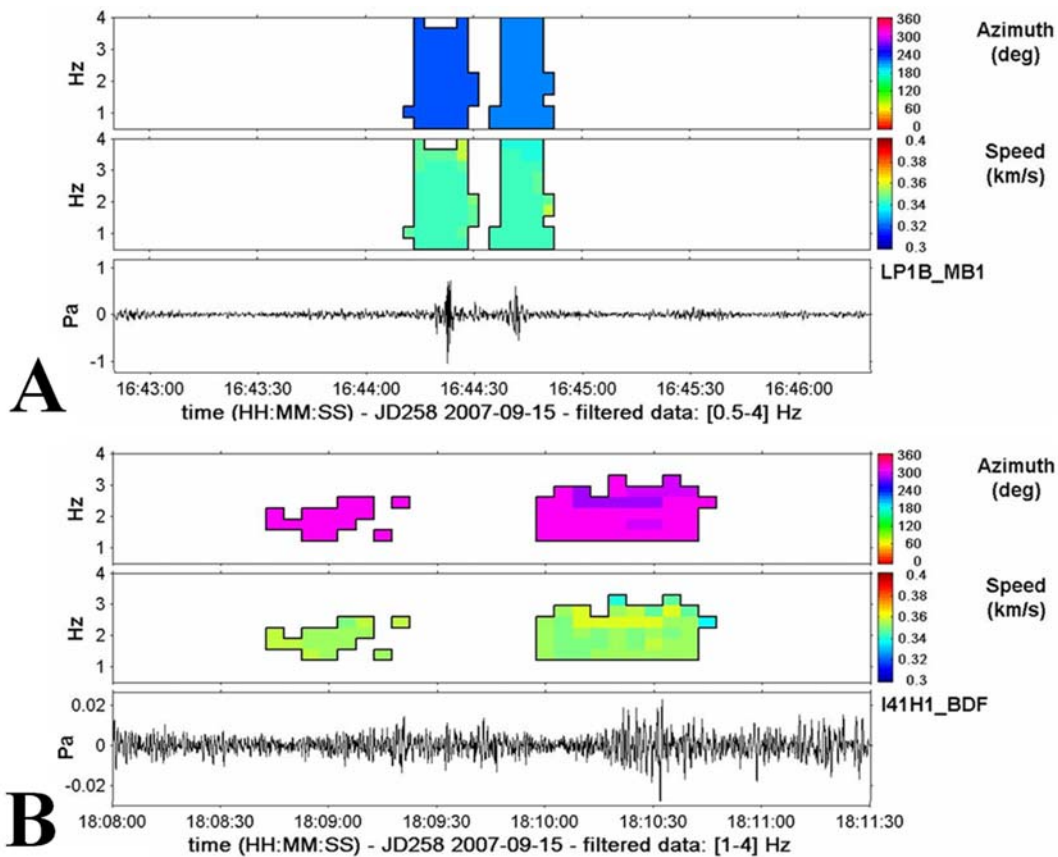| Station	Arrival time (UTC)	Back azimuth (°)	Trace velocity (km/s)	Celerity (km/s)	Peak-peak amplitude (Pa)	Dominant frequency (Hz)
I08BO	16:44:10	227.4	0.345	–	1.70	1.7
	16:44:34	214.6	0.344	–	0.86	1.2
I41PY	18:08:51	309.0	0.354	0.305	0.02	1.1
	18:10:10	308.5	0.352	0.3	0.04	1.6

Fig. 4. Results of PMCC calculation for infrasound recordings at I08BO (A) and I41PY (B). Data are filtered from 0.5 to 4 Hz and 1 to 4 Hz for I08BO and I41PY, respectively, in 10 equally spaced frequency bands. Detection results are presented on a same time scale of 210 s. Color scales indicate values of back-azimuth (in degrees, with respect to north site) and horizontal trace velocity (in km/s). The main characteristics of the detected coherent signals are listed in Table 3.
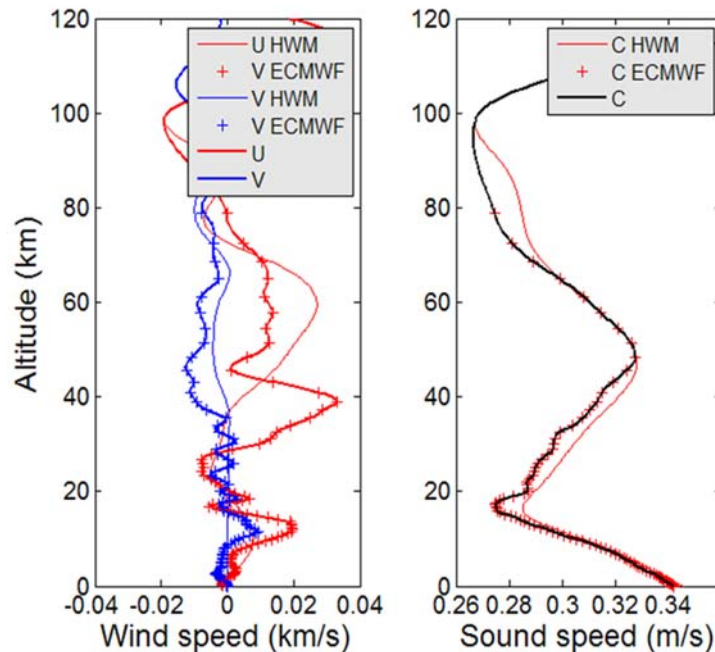

Fig. 5. Atmospheric conditions on September 15, 2007, at 18:00 UTC for coordinates 16.66°S and 69.04°W. The zonal and meridional winds (U and V, respectively), sound speed profiles (C) are provided by the MSIS-90 and HWM-93 empirical atmospheric models and the 91 layers ECMWF model. The vertical profiles C, U, and V merge the HWM/MSIS climatologies with ECMWF data using B-spline functions.

ground level (~0.34 km/s above sea level and ~0.33 km/s at 4 km altitude). Given the effective sound speed profile (Fig. 5), at distance smaller than 100 km, none of the observed signals at I08BO can be associated with this ray family. The celerity values of the two coherent wave trains (0.33 and 0.30 km/s) and the corresponding azimuthal deviations relative to the true bearing in the direction of the crater (−4.3° and −15.1°) suggest that the detected signals at I08BO originated either from ballistic shock waves and/or fragmentation process just before the impact.

Source Model and Trajectory Reconstruction

The impact source location is calculated from the Pg and Sg direct crustal waves at stations BBOB, BBOD, BBOE, BBOK, and LPAZ (Table 2). A local seismic magnitude of 1.45 is derived from the seismic recordings. A clear low frequency wavetrain is observed on the closest station to the impact (BBOD) (Fig. 3), which is typical of shallow seismic events propagating in water-saturated soils. The back-azimuth of 246.3° calculated from the LPAZ three-component short-period station is consistent with energy originating from the crater. Using a standard non-linear least square inversion procedure (Coleman et al. 1996) and a two-layer regional velocity model, the following coordinates and impact time are derived: 16.64°S, 68.96°W, 8 km away from crater, at 16:40:16.7 UTC (Fig. 2). Cross-bearing localizations associating the first and second infrasound arrivals detected at I08BO and I41PY are also indicated on Fig. 2 (16.72°S, 69.02°W at 16:40:07, and 16.85°S, 68.89°W at 16:40:55, 7 and 26 km east of the crater, respectively). These two localizations account for uncertainties in the azimuth estimates due to transversal wind effects on the propagation (~5°). The observed coordinates of the crater (16.66°S, 69.04°W) and the impact origin time derived from the seismic localization (16:40:16.7 UTC) are considered here as ground truths. From this location, different sets of possible trajectories are explored by minimizing residuals between the observed and predicted arrival times of ground coupled airwaves.

The entry speed of a meteoroid has an upper limit. The Earth orbits the Sun at a mean speed of 30 km/s in a heliocentric referential in the apex direction, and the speed of a meteoroid with an elliptic orbit in the solar system cannot exceed 42 km/s (solar system escape velocity). Thus, the speed relative to the Earth can range from 0 km/s (from the antapex direction with a 30 km/s speed) to 72 km/s (frontal collision with the Earth). According to the time and location of the impact, the relative speed of the Carancas meteoroid can range from 0 km/s to 57 km/s. Moreover, the Earth escape velocity of 11.2 km/s defines the minimum initial speed of any meteoroidal object entering the atmosphere. This velocity is nearly constant when the object penetrates the upper layers of the atmosphere. Below the

altitude of 30 km, the meteoroid generally slows down as the altitude decreases (ReVelle et al. 2004). In a first approximation, we assume that the entry speed of the studied event is 20 km/s above 30 km, and then linearly decreases with the altitude down to 1 km/s. Due to the contrast between the meteoroid supersonic speed and the sound speed, the infrasound measurements alone could not yield more precise values for the entry velocity. The travel time of the infrasonic waves mainly depends on the vertical structure of the wind and temperature profiles. Consequently, the solutions found using different initial and final supersonic speeds of the meteoroid always range within the uncertainty bounds indicated below.

With such a speed model, the rectilinear trajectory is only defined by its elevation and azimuthal angles. On the basis of the existing visual reports, the elevation (relative to the horizontal) and azimuthal angles (clockwise from North) range from 10 to 80° and −50 to 170°, respectively. We focus on the two clear arrivals observed at stations I08BO, BBOD, BBOE and BBOK, which are likely related to the same origin. In order to explain the observed time sequences of acoustic arrivals, ray paths and travel times are computed using the Tau-P ray tracing code (Garcés et al. 1998) for each point of the trajectory using the atmospheric conditions presented in Fig. 5.

At supersonic speeds, pressure waves combine and form a Mach cone radiating away from the generation point (ReVelle 1976). At several tens of kilometers from the bolide, signals do not exhibit the typical N-wave signature, but rather appear in the form of observed pulses (Pierce and Maglieri 1972). We first assume that the detected airwaves propagated in a direction normal to the Mach cone whose opening angle β is given by $\sin(\beta) = C_z/V_z$, where C_z and V_z, are respectively the sound and meteoroid speeds at the altitude z. In our simulations, rays are launched at different angles determined both by the speed and trajectory of the bolide, and the ECMWF sound speed profile. The source is thus approximated by a linear distribution of elementary Mach cones. Waves normal to the Mach cones are defined by unique azimuthal and elevation angles (Le Pichon et al. 2002b). For stations I08BO, BBOD, BBOE, and BBOK (I41PY, ~1600 km away from the source, is discarded due to large uncertainties in travel time calculations), the minimum time residual is found to be less than 5 s for a east-westwards (azimuth = 100 ± 30°) trajectory with a 40 ± 3° elevation angle (Fig. 6A). However, the results do not predict more than one arrival at all stations. Furthermore, such source model can not explain the infrasound arrivals at I41PY station, as the front wave propagates nearly perpendicularly to the trajectory of the fireball. Finally, the large azimuth residuals (greater than 50°) indicate that this trajectory is far from being the most plausible.

We also make the simplifying assumption that the detected signals were generated by two main thermal blasts radiating isotropically. The minimum time residual is then
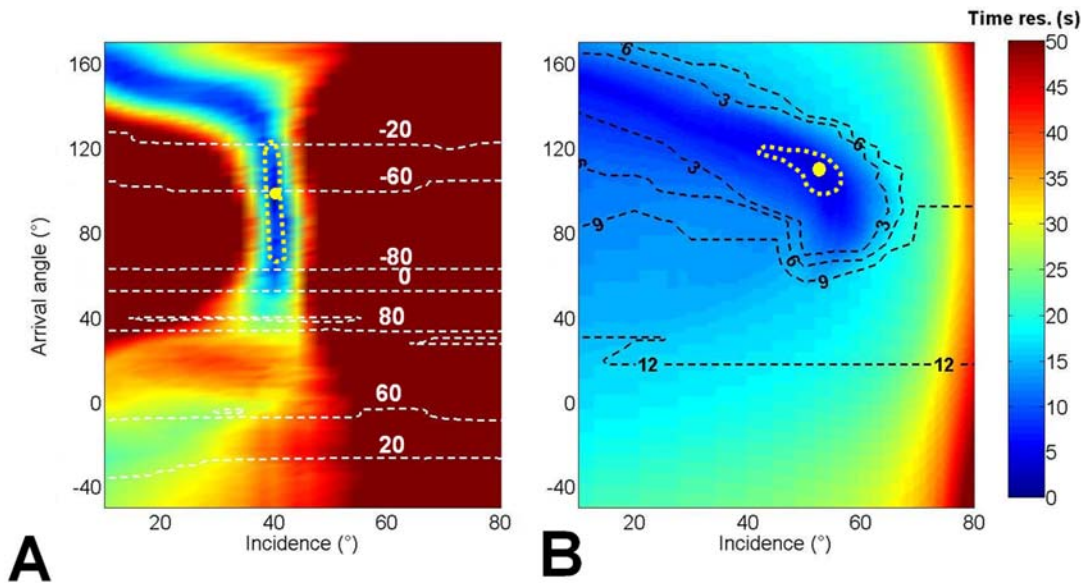
Fig. 6. Time (colormap) and back-azimuth (contour lines) residuals calculated for different sets of trajectories. A trajectory is defined by its arrival and incident angles. For each set of arrival and incidence angles, rays are launched for 100 points along the trajectory. The mean arrival time residuals (in seconds) account for the two arrivals detected at BBOB, BBOK, BBOE, and I08BO. The arrival time and back-azimuth residuals are calculated using two different models: A) propagation normal to the Mach cone, B) point-like sources mimicking the two fragmentations. The yellow dots indicate the minimum of the arrival time residuals. The yellow contour lines outline the area where these residuals are lower than 5 s. The back-azimuth residuals (in degrees) are calculated for the points along the trajectories that minimize the time residuals.

found for two fragmentations occurring at altitudes of 21 ± 2 km and 31 ± 2 km above the ground level, along a trajectory of azimuth $110 \pm 20°$ and elevation $50 \pm 10°$ (Fig. 2 and 6B). Figure 3 compares the observed arrival times to the predicted ones. This approach explains both the arrival times of the two onsets detected at I08BO, BBOD, BBOE, and BBOK with a mean residual of 5 s, as well as the detected back-azimuths at I08BO with a maximum error of 2° (Fig. 6B). The time difference between signals at BBOE and BBOK corroborate this path (Fig. 3). At a horizontal distance of 70–75 km from the fragmentations, simulations predict shallow elevation angles for rays reaching I08BO, with celerity values consistent with the observed ones.

Long-Range Propagation

Infrasound propagation is significantly affected by the vertical and horizontal wind structure where wind-induced refraction can trap or disperse sound energy. Advances in parabolic equation methods recently provided a new tool for studying atmospheric infrasound propagation at local and regional scales using enhanced atmospheric specifications. In order to gain additional physical insight into the observed signals at I41PY, simulations are carried out using a wide angle and high Mach number parabolic equation for sources radiated isotropically located at different altitudes (Lingevitch et al. 2002). The Naval Research Laboratory Ground-to-Space (NRL-G2S) model (Drob et al. 2003) includes recent atmospheric data sets, improved

parameterization of the atmospheric vertical structure, and capabilities for near-real time global assimilation of tropospheric and stratospheric winds. In order to get accurate simulation results, the NRL-G2S model was run to provide a self-consistent atmospheric specification (sound velocity and wind speed profiles) for September 15, 2007, at 16:00 UTC, over a grid of 0.5×0.5 degree, from ground level to 150 km altitude, with a vertical resolution is 0.25 km. Figure 7 presents the simulation results for source altitudes ranging from 10 to 50 km at a frequency of 1 Hz. As expected, thermospheric returns are strongly attenuated and are not measurable over such long range. A dominant elevated stratospheric waveguide is observed between 10 and 35 km. A small fraction of the stratospheric energy bounces on the Earth's surface and reaches the infrasound array. Assuming a point-like source model, the signal attenuation is larger than 70 dB for a source altitude below 10 km and above 50 km. The source altitude should thus range between 10 and 40 km where a much weaker attenuation is predicted (~40 dB).

For these arrivals, ray tracing predicts back-azimuth corrections lower than 2° due to the transverse wind component which slightly deflects the rays from the original launch direction. At 20 km altitude, the predicted celerity values for the two signals (0.295 to 0.305 km/s) are consistent with the observed ones (0.305 and 0.300 km/s) (Fig. 4). The observed horizontal trace velocities (0.354 and 0.352 km/s, Table 3), are also consistent with the simulated ones. Such celerity and trace velocity values are typical of a stratospheric propagation (Brown et al. 2002). According to these
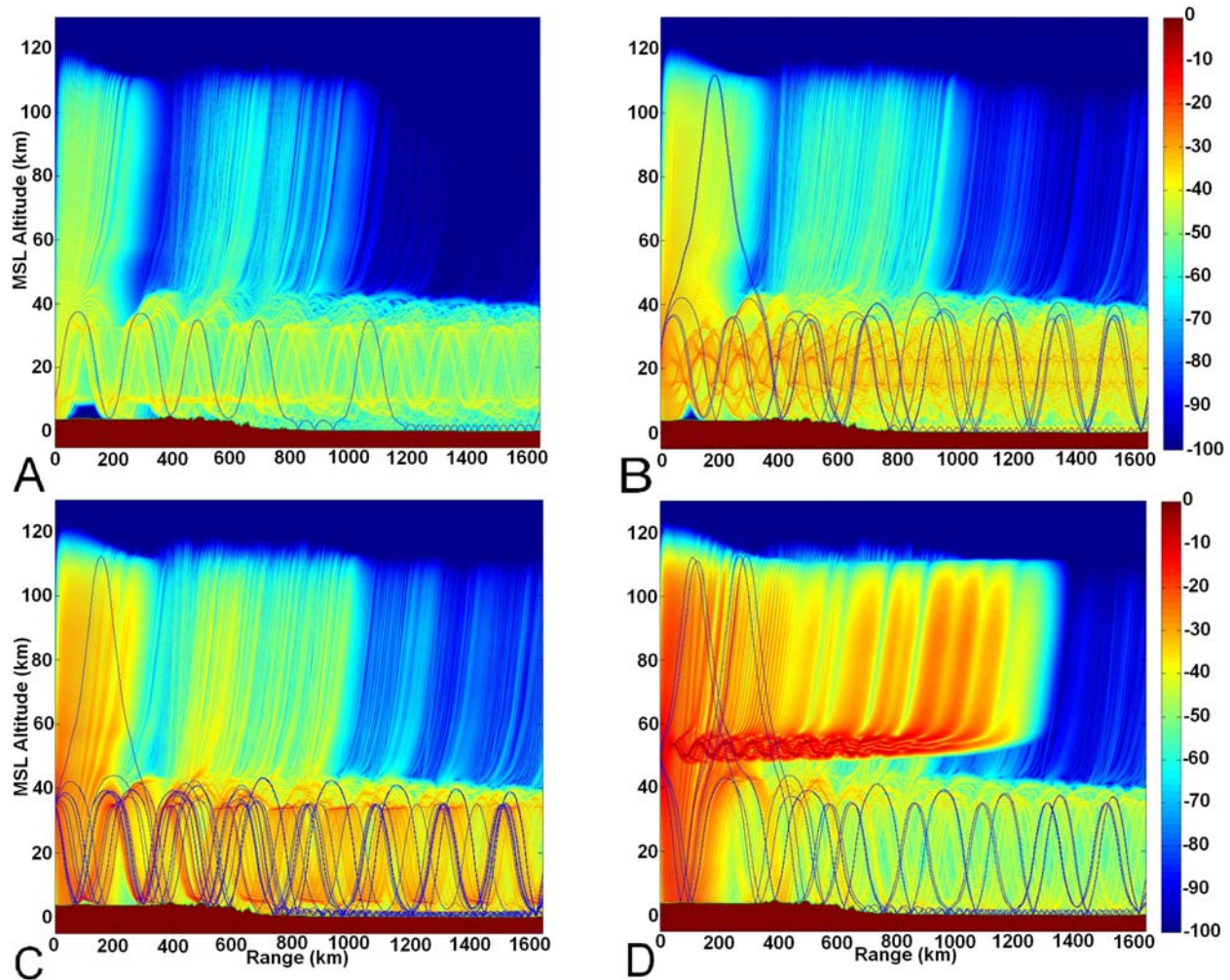
Fig. 7. Propagation of infrasonic waves in the direction of I41PY for different source heights (A, B, C, D: 10, 25, 35, and 50 km, respectively) and a frequency of 1 Hz. The NRL-RAMPE parabolic equation method (Lingevitch et al. 2002) combined with the environmental profiles derived from the G2S atmospheric model are compared to a 3D ray traces adapted from the Tau-P method (Garcés et al. 1998). Since effects of the boundary conditions of the propagation domain are particularly important in the high-altitude Andes region, simulations account for the NOAA Global Land One-km Base Elevation (GLOBE) digital terrain elevation model (Hastings and Dunbar 1998). According to these simulations, the recorded signals at I41PY can be explained by multiple stratospheric returns.

simulations, the two coherent wave trains at I41PY can either be interpreted as two consecutive stratospheric returns or be associated with the two fragmentations discussed above.

SIZE AND ENERGY ESTIMATION

Using a drastic simplification, a massive body penetrating the atmosphere with a velocity considerably greater than the speed of sound instantaneously looses a large part of its kinetic energy during ablation process (Ceplecha et al. 2005). It suffers such a strong deceleration that it fragments before reaching the ground surface. The explosive energy released by the two fragmentations is calculated by applying semi-empirical relations based on the infrasonic recordings at I08BO and I41PY. The most striking effect of the sudden release of the remaining kinetic energy is the

formation of the crater. From the observed crater diameter and the total ejected volume, the equivalent explosive energy released by the impact, the mass and diameter of the impactor are evaluated.

Explosive Energy

As used by Evers et al. (2001), the explosive energy released by fragmentation can be calculated by applying the following semi-empirical relation based on infrasonic recordings from low-altitude nuclear explosions (Whitaker et al. 1995; ReVelle 1997):

$$\log_{10}(E_s/2) = 3.34 \log_{10}\left(\frac{1}{f_{obs}}\right) - 2.58 \qquad (1)$$

where f_{obs} is the dominant frequency at the maximum

Table 4. Possible Carancas meteoroid orbital parameters. Those orbital parameters solutions for the Carancas meteoroid are calculated using different initial entry speed V: a is the semi-major axis, e is the eccentricity, and i the inclination of the orbit. The parent bodies are the objects with orbit similar to the modelled one.

Orbit_ID	V (km/s)	a (AU)	e	i (°)	Potential parent body
–	1.00	0.9577	0.061	0.5423	None
–	2.00	0.9199	0.1101	1.111	None
–	3.00	0.8868	0.1579	1.709	None
1	4.00	0.8577	0.2041	2.337	2007 RO17
2	5.00	0.8319	0.2478	2.998	2002 CW11
3	6.00	0.8091	0.2918	3.695	2003 SW130, 2004 FH, 2005 YR3, 2006 QQ23
4	7.00	0.7890	0.3333	4.430	2002 JX8, 2006 SE6
5	8.00	0.7711	0.3732	5.207	2006 SE6, 2007 DB61
6	9.00	0.7554	0.4116	6.028	2007 VB138, 2007 WM3
7	10.00	0.7415	0.4485	6.897	1998 WT24, 2007 PS25, 2007 WM3

amplitude (in Hz) and E_s represents the energy (in kilotons of a TNT equivalent explosion) limited to $E_s < 100$ kt. Using the above relation, with the measured frequencies listed in Table 3, the yield of the fragmentation ranges from 0.9 to 2.9 tons TNT (I08BO), and from 1.1 to 3.8 tons TNT (I41PY).

An important parameter for event characterization is also the amplitude. Actually, atmospheric winds strongly affect the recorded signals. Edwards et al. (2006) examined the correlation between infrasonic amplitude and yield, and derived the following expression:

$$W = 10^{3(a-kVs)/b} R^3 A^{-3/b} \qquad (2)$$

where R is the source to receiver range (in km), A is the maximum peak-to-peak amplitude (in Pa), V_s is the velocity of the stratospheric wind in the source-receiver direction (in m/s), and (a, b, k) are empirical constants (Mutschlecner et al. 1990). Edwards et al. (2006) had to distinguish between small and large bolides to find their regression fits. Assuming that the energy released by each fragmentation is lower than 7 kt (which is highly probable according to the previous calculations), the constants are: $a = 3.36 \pm 0.60$, $b = -1.74 \pm 0.24$ and $k = -0.0177$ s/m. At a distance of 1617 km, I41PY recorded stratospheric arrivals of amplitude 0.02 and 0.04 Pa (Table 3). Using these values and a constant effective stratospheric wind of 30 m/s, a yield of 1.0 to 3.2 tons TNT is found. These yield estimates derived from two independent empirical approaches are here in reasonable agreement.

Meteoroid Diameter

Holsapple (1993) reviewed the scaling laws for impact processes and related the mass and velocity of the impactor to the crater size and type of soil. In the strength regime, the strength of the soil is large compared to the lithostatic pressure, thus the latter can be ignored. This assumption is valid for meter-sized objects. For a crater in wet soil in the strength regime, Holsapple (1993) derived:

$$L \propto 0.05 \, m \, V^{1.65} \qquad (3)$$

where L is the crater volume (in m³), m is mass of the

impactor (in kg), and V its speed (in km/s). With a depth of 5 m and a mean diameter of 13.5 m, a total ejected volume of 480 m³ (half-volume of an ellipsoid) is estimated. For an impact speed ranging from 0.8 to 3 km/s, the mass of the meteoroid ranges between 1.5 and 15 tons. With a chondritic density of 3.5 (relative to water), a corresponding meteoroid diameter between 1 and 2 m is calculated. Since only objects of diameter greater than one meter are able to touch down (Brown et al. 1996), such values are acceptable.

Energy Released by the Impact and Speed Estimates

The yield of an explosion can be determined based on the crater size. Glasstone (1957) used crater sizes of nuclear tests of yield W, in the range of 1 to 20,000 kT TNT, and derived that the diameter scales with $W^{1/3}$, and the depth with $W^{1/4}$. Kinney et al. (1985) used 200 large surface explosions and found that the crater diameter d scales with the explosive yield W in kg TNT as:

$$d = 0.8 \, W^{1/3} \qquad (4)$$

Using the above relation and the reported crater diameter (Fig. 1), the yield is determined as 4.8 tons. It is noteworthy that in this case, the crater is caused by a moving object impacting on the Earth's surface rather than an explosive point source.

Considering that during the impact, in addition to thermal losses, a fraction of the kinetic energy is transmitted through the soil and the atmosphere, a speed lower limit of the impactor can be estimated from the kinetic energy E_k formula,

$$E_k = \frac{1}{2}\rho\left(\frac{\pi d^3}{6}\right)V^2 \qquad (5)$$

where ρ is the density (in kg/m³), d is the diameter of the meteoroid (in m), and V is the speed (in m/s). According to this relation, the lowest terminal speed is 1.5 km/s, which is consistent with the velocity model defined in the section Source Model and Trajectory Reconstruction.

From the time of occurrence of the two fragmentations, the estimated trajectory, the airwaves arrival times at stations

Table 5. Orbital elements (semi-major axis *a*, eccentricity *e*, and inclination *i*) of possible parent bodies (Source: NASA/JPL/HORIZONS).

Body_ID	Name	*a* (AU)	*e*	*i* (°)
1	2002 CW11	0.8656	0.2256	3.133
2	2002 JX8	0.7701	0.3053	4.316
3	2003 SW130	0.8849	0.3034	3.666
4	2004 FH	0.8179	0.2891	0.021
5	2005 YR3	0.8185	0.2727	3.607
6	2006 QQ23	0.8038	0.2845	3.440
7	2006 SE6	0.8052	0.3455	4.818
8	2007 DB61	0.8114	0.3642	5.372
9	2007 PS25	0.7287	0.4215	6.719
10	2007 RO17	0.9265	0.1970	2.465
11	2007 VB138	0.7723	0.4311	6.038
12	2007 WM3	0.7942	0.4283	6.431
13	1998 WT24	0.7185	0.4180	7.342

Table 6. D-criteria between different meteoroid orbits (Orbit_ID, Table 4) and possible parent bodies (Body_ID, Table 5). The calculations were carried for possible parent bodies whose Drummond criterion is less than 0.1 (DD = Drummond criterion, DSH = Southworth and Hawkins criterion).

V (km/s)	Orbit_ID	Body_ID	D-criterion	Comments on evolution
4.00	1	10	0.06778 (DD)	Different
5.00	2	6	0.08308 (DD)	Different
6.00	3	6	0.09053 (DSH)	Different
6.00	3	6	0.03155 (DD)	Different
7.00	4	6	0.09625 (DD)	Totally different
7.00	4	7	0.04624 (DD)	Similar
8.00	5	7	0.07291 (DD)	Similar
9.00	6	9	0.07422 (DD)	*a* shifted by 0.03 AU, *e* shifted by 0.01, *i* different
10.00	7	9	0.08079 (DD)	*a* shifted by 0.01 AU, *e* shifted by 0.02, *i* different

BBOD, BBOE, and BBOK, and the predicted Tau-P travel times, a maximum speed of 10 km/s is evaluated below 27 km altitude. In the first upper layers of the atmosphere above 30 km, the speed of the meteoroid is nearly constant (ReVelle et al. 2004). Therefore, with an entry speed of 11.2 km/s, a meteoroid diameter of 2–4 m before ablation and a chondritic density of 3.5, the initial energy released would range from 1 to 8 kt TNT equivalent. More observations would certainly reduce the upper limit source energy, yielding a more realistic estimate of the initial kinetic energy.

CONCLUDING REMARKS

The terrestrial impact of the Carancas meteoroid near the Bolivian border with Peru has been detected by the Bolivian seismic network at a range of 125 km. At a distance of 1617 km from the crater, along the dominant stratospheric wind direction, infrasonic waves are associated with the entry of the meteoroid. Ray tracing simulations based on a supersonic moving point source, consider both shock waves generated by an almost cylindrical line emission and acoustic emission from point-like explosions. The conclusion of this analysis is that fragmentations were probably the dominant process in the production of sound during the entry, rather than the hypersonic shock of the meteoroid passage through the

atmosphere. Mean residuals between the predicted and observed arrival times indicate that the strongest infrasonic signals probably originated from two main thermal bursts at altitudes of 25 and 35 km above sea level, along a trajectory of azimuthal angle 110° and elevation 50°. The back-azimuth and elevation angles of the two coherent wave trains detected at I08BO are consistent with the location and time of occurrence of these fragmentations. This path corroborates the apparent trajectory reported at the town of Desaguadero. Moreover, a recent and independent study by Brown et al. (2008) yields similar results derived from different set of data.

On the basis of the recorded signals at I08BO and I41PY, consistent yield estimates of the fragmentations are derived from independent empirical approaches. The explosive energy released by the two fragmentations is evaluated between 1.0 and 3.8 t TNT equivalent each. From the crater diameter and the total ejected volume, a rock of 1 to 2 meter-diameter would have released an explosive energy of 4.8 tons TNT. The detailed analysis of the seismic and infrasound recordings suggests a rather low initial entry speed of the meteoroid (~12 km/s) which may explain why it survived its atmospheric entry without major fragmentation before impacting the Earth.

The orbital parameters of the object can be deduced from the trajectory and the initial entry speed. This naturally raises

the question whether the meteoroid could be a fragment of an asteroid or comet. In order to associate two celestial bodies, we computed the similarity between orbital elements using the D-criterion methods proposed by Southworth and Hawkins (1963) and Drummond (1981). The initial velocity is here a crucial parameter. From the estimated trajectory, the orbital parameters of the Carancas bolide were calculated at 30 km altitude. We then consider velocity values ranging from 1 km/s to 10 km/s with a 1 km/s step, and create ten sets of orbital elements (Table 4). The possible parent bodies are first selected from the NASA Jet Propulsion Laboratory (JPL) HORIZONS database (http://ssd.jpl.nasa.gov/) with asteroids and comets of similar orbital elements (Table 5). Out of the 13 objects found, only 4 bodies have a Drummond criterion less than 0.1 (Table 6). The dynamical study of each solution considering all potential parent bodies was performed by integrating their orbital parameters on a 5,000 year period, taking into account gravitational influences of the planets, as well as non-gravitational forces. Unfortunately, given the uncertainties in the trajectory and energy estimates, we can not definitely confirm any association. Further studies gathering additional measurements, such as visual observations, could reduce ranges of uncertainty in estimating the initial speed and size of the object, and would thus help in associating it with a known celestial source.

According to the existing statistics and observations, such an event happens every few years (Toon et al. 1997; Chyba et al. 1998; Brown et al. 2002b). This work applies to a natural event using various technical and analytical detection methods developed with the aim of monitoring the CTBT. It demonstrates the value of seismo-acoustic synergy to obtain precise location of a naturally occurring source. With the increasing number of IMS and regional cluster of seismo-acoustic networks deployed around the globe, along with a continuation of research in the field of infrasound monitoring, meteoroid entry evidences would probably occur more frequently in the next years. It is also expected that the development of enhanced near real-time atmospheric specifications and new propagation modeling capabilities will improve our knowledge of meteoroid characteristics.

Editorial Handling—Dr. Donald Brownlee

REFERENCES

Alarcón H. B. and Gorinova E. 2007. Estudio Microscopico del Meteorito de Huanu Collo. Instituto de Investigaciones Geológicas y del Medio Ambiente—Carrera "Fisica." Fac. De Ciencias Puras—UMSA Planetario Max Schreier, 8 p. http://fcpn.umsa.bo/fcpn/app?service=external/Planetarium_Area View&sp=241.

Alcoverro B. and L. Pichon A. 2005. Design and optimization of a noise reduction system for infrasonic measurements using elements with low acoustic impedance. *Journal of the Acoustical Society of America* 117, doi:10.1121/1.1804966.

Arrowsmith S. J., Drob D. P., Hedlin M. A. H., and Edwards W. 2007. A joint seismic and acoustic study of the Washington State bolide: Observations and modeling. *Journal of Geophysical Research* 112, D09304, doi:10.1029/2006 JD008001.

Beech M., Brown P., Hawkes R. L., Ceplecha Z., Mossman K., and Wetherhill G. 1995. The fall of the Peekskill meteorite: Video observations, atmospheric path, fragmentation record and orbit. *Earth, Moon, and Planets* 68:189–197.

Brown D. J., Katz C. N., Le Bras R., Flanagan M. P., Wang J., and Gault A. K. 2002. Infrasonic signal detection and source location at the Prototype Data Centre. *Pure and Applied Geophysics* 159:1081–1125.

Brown P., Hildebrand A. R., Green D., Page D., Jacobs C., ReVelle D. O., Tagliaferri E., Wacker J., and Wetmiller B. 1996. The fall of the St-Robert meteorite. *Meteoritics & Planetary Science* 31:502–517.

Brown P., ReVelle D. O., Tagliaferri E., and Hildebrand A. R. 2002a. An entry model for the Tagish Lake fireball using seismic, satellite and infrasound records. *Meteoritics & Planetary Science* 37:661–675.

Brown P., Spalding R. E., ReVelle D. O., Tagliaferri E., and Worden S. P. 2002b. The flux of small near-Earth objects colliding with the Earth. *Nature* 420:294–296.

Brown P., Kalenda P., ReVelle D. O., and J. Borovička 2003. The Morávka meteorite fall: 2. Interpretation of infrasonic and seismic data. *Meteoritics & Planetary Science* 38:989–1003.

Brown P., Pack D., Edwards W. N., ReVelle D. O., Yoo B. B., Spalding R. E., and Tagliaferri E. 2004. The orbit, atmospheric dynamics, and initial mass of the Park Forest meteorite. *Meteoritics & Planetary Science* 39:1781–1796.

Brown P., ReVelle D. O., Silber E. A., Edwards W. N., Arrowsmith S., Jackson L. E., Tancredi G., and Eaton D. 2008. Analysis of a crater forming meteorite impact in Peru. *Journal of Geophysical Research* 113 (E09007), doi:10.1029/2008JE003105.

Cansi Y. 1995. An automatic seismic event processing for detection and location: The PMCC method. *Geophysical Research Letters* 22:1021–1024.

Cates J. E. and Sturtevant B. 2002. Seismic detection of sonic booms. *Journal of the Acoustical Society of America* 111:614–628.

Ceplecha Z., Brown P., Hawkes R. L., Wetherill G., Beech M., and Mossman K. 1996. Video observations, atmospheric path, orbit and fragmentation record of the fall of the Peekskill meteorite. *Earth, Moon, and Planets* 72:395–404.

Ceplecha Z. and ReVelle D. O. 2005. Fragmentation model of meteoroid motion, mass loss, and radiation in the atmosphere. *Meteoritics & Planetary Science* 40:35–54.

Chyba C. F., Van Der Vink G. E., and Hennet C. B. 1998. Monitoring the Comprehensive Test Ban Treaty: Possible ambiguities due to meteorite impacts. *Geophysical Research Letters* 25:191–194.

Coleman T. F. and Li Y. 1996. An interior, trust region approach for

nonlinear minimization subject to bounds. *SIAM Journal on Optimization* 6:418–445.

Drob D., Picone J. M., and Garcés M. 2003. The global morphology of infrasound propagation. *Journal of Geophysical Research* 108, doi:10.1029/2002JD003307.

Drummond J. D. 1981. A test of comet and meteor shower associations. *Icarus* 45:545–553.

Edwards W. N, Brown P. G., and ReVelle D.O. 2006. Estimates of meteoroid kinetic energies from observations of infrasonic airwaves. *Journal of Atmospheric and Solar-Terrestrial Physics* 68:1146–1160.

Evers L. G. and Haak H. W. 2001. Listening to sounds from an exploding meteor and oceanic waves. *Geophysical Research Letters* 2:41–44.

Garcés M., Hansen R. A., and Lindquist K. G. 1998. Travel times for infrasonic waves propagating in a stratified atmosphere. *Geophysical Journal International* 135:255–263.

Garcés M., Drob D. P., and Picone J. M. 2002. A theoretical study of the effect of geomagnetic fluctuations and solar tides on the propagation of infrasonic waves in the upper atmosphere. *Geophysical Journal International* 148:77–87.

Glasstone S. 1957. *The effect of nuclear weapons.* U. S. Atomic Energy Commission. Washington, D. C. 196–227.

Hastings D. A. and Dunbar P. K. 1998. Development and assessment of the Global Land One-km Base Elevation Digital Elevation Model (GLOBE). *International Society of Photogrammetry and Remote Sensing* 32:218–221.

Hedin A. E. 1991. Extension of the MSIS thermosphere model into the middle and lower atmosphere. *Journal of Geophysical Research* 96:1159–1172.

Hedin A. E., Fleming E. L., Manson A. H., Schmidlin F. J., Avery S. K., Clark R. R., Franke S. J., Fraser G. J., Tsuda T., Vial F., and Vincent R. A. 1996. Empirical wind model for the upper, middle and lower atmosphere. *Journal of Atmospheric and Terrestrial Physics* 58:1421–1447.

Holsapple K. A. 1993. The scaling of impact processes in planetary sciences. *Annual Review of Earth and Planetary Sciences* 21: 333–373.

Kinney G. F. and Graham K. J. 1985. *Explosive shocks in air.* New York: Springer-Verlag. pp. 9–10.

Krinov E. L. 1971. New studies of the Sikhote-Alin iron meteorite shower. *Meteoritics* 6:127–138.

Kulichkov S. N. 1992. Long-range propagation of sound in the atmosphere: A review. *Izvestiia Russian Academy of Sciences, Atmospheric Oceanic Physics* 28:339–360.

Le Pichon A., Guérin J. M., Blanc E., and Raymond D. 2002a. Trail in the atmosphere of the December 29, 2000, meteorite as recorded in Tahiti: Characteristics and trajectory reconstitution. *Journal of Geophysical Research* 107, doi:1029/2001JD001283.

Le Pichon A., Garcés M., Blanc E., Barthélémy M., and Drob D. P. 2002b. Acoustic propagation and atmosphere characteristics derived from infrasonic waves generated by the Concorde. *Journal of the Acoustical Society of America* 111:629–641.

Lingevitch J. F., Michael C., Dalcio D., Douglas D., Joel R., and William S. 2002. A wide angle and high Mach number parabolic equation. *Journal of the Acoustical Society of America* 111, doi: 10.1121/1.1430683:729–734.

Macedo L. F. and Macharé J. O. 2007. The Carancas meteorite fall, 15 September 2007. Official INGEMMET initial report. 5 p.

Minaya E., Rougon P., Valero D., Fernandez G., Lazaro E., and Cano W. 2007. The Bolivian Seismic Network (abstract S34A-02). 2007 American Geophysical Union Joint Assembly. *Eos Transactions* 88.

Mutschlecner J. P. and Whitaker R. W. 1990. The correction of infrasound signals for upper atmospheric winds. Proceedings, 4th International Symposium on Long-Range Sound Propagation. pp.143–153.

Oberst J., Heilein D., Köhler U., and Spurný P. 2004. The multiple meteorite fall of Neuschwanstein: Circumstances of the event and meteorite search campaigns. *Meteoritics & Planetary Science* 39:1627–1641.

Pierce A. D. and Maglieri D. J. 1972. Effects of atmospheric irregularities on sonic-boom propagation. *Journal of the Acoustical Society of America* 51:702–720.

ReVelle D. O. 1976. On meteor-generated infrasound. *Journal of Geophysical Research* 81:1217–1230.

ReVelle D. O. 1997. Historical detection of atmospheric impacts of large super-bolides using acoustic-gravity waves. *Annals of the New York Academy of Sciences* 822:284–302.

ReVelle D. O., Whitaker R. W., and Armstrong W. T. 1998. Infrasound from the El Paso super-bolide of October 9, 1997 (abstract). SPIE Conference on Characteristics and Consequences of Space Debris and Near-Earth Objects, San Diego, California, USA.

ReVelle D. O., Brown P. G., and Spurný P. 2004. Entry dynamics and acoustics/infrasonic/seismic analysis for the Neuschwanstein meteorite fall. *Meteoritics & Planetary Science* 39:1605–1626.

Southwork R. B. and Hawkins G. S. 1963. Statistics of meteor streams. *Smithsonian Contributions to Astrophysics* 7:261–285.

Sutherland L. C. and Bass H. E. 2004. Atmospheric absorption in the atmosphere up to 160 km. *Journal of the Acoustical Society of America* 115:1012–1032.

Spurný P., Oberst J., and Heinlein D. 2003. Photographic observations of Neuschwanstein, a second meteorite from the orbit of the Příbram chondrite. *Nature* 423:151–153.

Toon O. B., Turco R. P., and Covey C. 1997. Environmental perturbations caused by the impacts of asteroids and comets. *Annals of the New York Academy of Sciences* 822:401–402.

Whitaker R. W. and ReVelle D. O. 1995. Analysis of the acoustic conversion efficiency for infrasound from atmospheric entry of NEOs. Los Alamos National Laboratory Report LA-UR-95–4121.